Additive Manufacturing: Metallurgy, Cut Analysis & Porosity

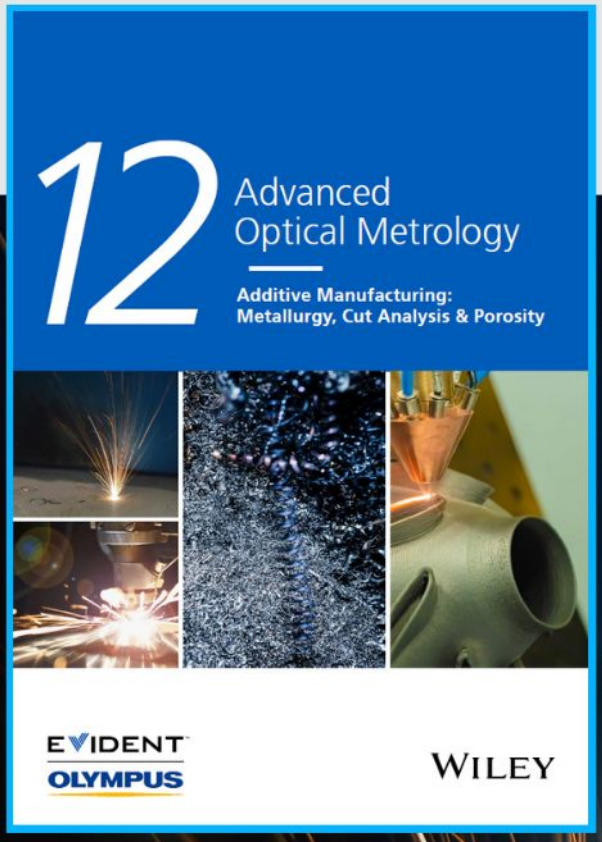

The latest eBook from Advanced Optical Metrology. Download for free.

In industry, sector after sector is moving away from conventional production methods to additive manufacturing, a technology that has been recommended for substantial research investment.

Download the latest eBook to read about the applications, trends, opportunities, and challenges around this process, and how it has been adapted to different industrial sectors.

EVIDENT
OLYMPUS

WILEY

NANO · MICRO small
www.small-journal.com

Ni Single Atoms on MoS_2 Nanosheets Enabling Enhanced Kinetics of Li-S Batteries

Chenxu Dong, Cheng Zhou, Yan Li, Yongkun Yu, Tianhao Zhao, Ge Zhang, Xinhui Chen, Kaijian Yan, Liqiang Mai, and Xu Xu**

The practical application of Li-S batteries is seriously hindered due to its shuttle effect and sluggish redox reaction, which requires a better functional separator to solve the problems. Herein, polypropylene separators modified by MoS_2 nanosheets with atomically dispersed nickel (Ni-MoS_2) are prepared to prevent the shuttle effect and facilitate the redox kinetics for Li-S batteries. Compared with pristine MoS_2 nanosheets, Ni-MoS_2 nanosheets exhibit both excellent adsorption and catalysis performance for overcoming the shuttle effect. Assembled with this novel separator, the Li-S batteries exhibit an admirable cycling stability at 2 C over 400 cycles with 0.01% per cycle decaying. In addition, even with a high sulfur loading of 7.5 mg cm^{-2}, the battery still provides an initial capacity of 6.9 mAh cm^{-2} and remains 5.9 mAh cm^{-2} after 50 cycles because of the fast convention of polysulfides catalyzed by Ni-MoS_2 nanosheets, which is further confirmed by the density functional theory (DFT) calculations. Therefore, the proposed strategy is expected to offer a new thought for single atom catalyst applying in Li-S batteries.

1. Introduction

People are facing serious energy crisis because the traditional fossil energy is increasingly consumed and newly developed renewable energy is hard to store.[1] Therefore, it is greatly required for human beings to develop advanced electrical energy storage systems. Lithium-ion batteries are limited by their energy density (140–260 Wh kg^{-1}) and high cost, which can't satisfy our requirement for electrical vehicles, portable electronics and so on.[2,3] Accordingly, lithium-sulfur (Li-S) batteries have drawn increasing attention as a promising substitute for energy storage devices on account of high capacity (1675 mAh g^{-1}) and theoretical energy density (2600 Wh kg^{-1}), as well as low-cost, earth abundance, and environmental friendliness of sulfur.[4–6] However, Li-S batteries suffer from several problems such as non-conductivity of sulfur, growth of lithium dendrites and the shuttle effect, impeding the process of commercialization.[7–10] In principle, people generally regard shuttle effect is the core problem that results in the poor cycle performance. For the shuttle effect, the soluble polysulfides from the sulfur cathode dissolve into the electrolyte, shuttle to the anode, and react with the lithium metal, which leads to the rapid capacity fading, low Coulombic efficiency, and a short cycle life. In addition, the polysulfides hinder the electron transport during the electrochemistry process, which brings about sluggish conversion of polysulfides and low sulfur utilization.[11–15] Consequently, it is highly desired to explore an effective strategy to prevent the shuttle effect and facilitate the redox kinetics.

Separators play an important role in batteries that facilitates ion transportation, blocks electron and avoids short circuit. Nevertheless, unmodified separators are not able to retard the diffusion of the polysulfides. In recent years, numerous researches have been conducted to investigate functional separators to confine polysulfides and promote kinetics process of the transformation from the immobilized polysulfides to Li_2S (kinetics conversion of the immobilized lithium polysulfides). It is generally believed that the commercial separator modification by coating functional materials is the most effective approach to design functional separator, which is more convenient and cost-effective than the fabrication of the composite sulfur cathodes.[4,16–18] In the past decades, a series of materials and strategies have been explored to modify separators. Initially, carbon materials were widely used as coating materials to physically adsorb polysulfides due to their high porosity and surface area. Nevertheless, physical adsorption is so weak to some extent that the separation effect is limited. Then chemical adsorption as a more efficient method was developed to adsorb polysulfides because the chemical bonds are stronger to anchor the polysulfides and suppress the shuttle effect. The polar materials such as transition metal oxides, sulfides and nitrides usually possess chemical active sites to adsorb polysulfides. However, these materials possess weak catalytic performance so that the sluggish redox kinetics of polysulfides confined on the active coating has an adverse effect on the cycle performance of the Li-S batteries. Taking metal sulfides as an example, the

C. Dong, C. Zhou, Y. Li, Y. Yu, T. Zhao, G. Zhang, X. Chen, K. Yan, L. Mai, X. Xu
State Key Laboratory of Advanced Technology for Materials Synthesis and Processing
International School of Materials Science and Engineering
Wuhan University of Technology
Wuhan, Hubei 430070, P. R. China
E-mail: mlq518@whut.edu.cn; xuxu@whut.edu.cn
The ORCID identification number(s) for the author(s) of this article can be found under https://doi.org/10.1002/smll.202205855.

DOI: 10.1002/smll.202205855

existence of the chemical bonds between metal and sulfur leads to few catalytic sites. In this circumstance, some active materials with great catalytic performance are introduced to improve the redox kinetics. It is worth mentioning that these coatings with catalytic and adsorptive effect usually have the ability to adsorb polysulfides and then catalyze further reduction, which can greatly restrain the shuttle effect and accelerate the transformation kinetics of lithium polysulfides. Though these catalysts are significant for redox conversion of polysulfides, a mass of catalysts are required so that it will increase the mass ratio of separators in the Li-S batteries, which will result in a low energy density.[19–25]

Among these active materials, atomic-scale single atom catalysts (SACs) are promising in terms of maximum atom utilization, uniform active site structure, remarkable catalytic performances and unique advantage of ultrahigh performance-to-metal ratios.[26–30] Zhang et al. reported single nickel (Ni) atoms on nitrogen-doped graphene (Ni@NG) to modify the separator of Li-S batteries, which exhibits excellent rate performance and stable cycling life. Whereas, it was fabricated by an in situ pyrolysis strategy, which puts forwards high requirements for temperature that is hard to control. Li et al. prepared a bifunctional separator (MOF-based Co-SACs) via the layer-by-layer (LBL) assembly of 2D ultrathin Co-MOF, which achieved highly safe Li-S batteries.[31,32] However, their preparation methods are complicated and difficult to achieve the practical application. Herein, distributed single Ni atoms supported on MoS_2 nanosheets are designed to modify Li-S separators via a facile preparation method. MoS_2 nanosheets as an active metal sulfide material have already been used for separator modification, because they can provide chemical sites to adsorb and anchor polysulfides.[33] Meanwhile, MoS_2 nanosheets could facilitate the redox reaction but its catalytic sites are so few that the catalytic effect is weak, so we introduce atomically distributed Ni species to improve the catalytic performance, which is able to offer abundant actively catalytic sites to facilitate the redox reaction of polysulfides. Therefore, the Ni-MoS_2 functional separator (Ni-MoS_2@PP) can not only adsorb polysulfides to hold back the shuttle effect but also accelerate the conversion of lithium polysulfides. As a result, the Li-S batteries assembled with the Ni-MoS_2@PP functional separator endow excellent electrolyte uptake, mechanical property and thermal stability. Meantime, the batteries show fantastic electrochemical performance. The initial capacity at 2 C is 599 mAh g^{-1} and the capacity damping rate is as low as 0.01% per cycle after 400 cycles. Even with a high sulfur load of 7.5 mg cm^{-2}, 5.9 mAh cm^{-2} has been retained after 50 cycles.

2. Results and Discussion

The schematic of the working mechanism of Ni-MoS_2 nanosheets is exhibited in **Figure 1**. Single Ni atoms dispersed MoS_2 nanosheets are able to adsorb polysulfides and accelerate the conversion kinetics of lithium polysulfides due to the catalytic performance of Ni species. As shown in Figure S1a,b, Supporting Information, the Ni-MoS_2 shows a nano-flower like morphology composed of nanosheets, which is similar to the pure MoS_2 (Figure S2a,b, Supporting Information). The similar morphology can eliminate the influence of morphology on properties. The corresponding energy dispersive spectrometry (EDS) mapping images confirm the uniform distribution of element Mo, S, and Ni (Figure S3a–d, Supporting Information). As shown in **Figure 2**a, the TEM images of Ni-MoS_2 nanosheets have the lamellar structure, which is similar with MoS_2 nanosheets (Figure S4a,b, Supporting Information). The HRTEM image shows that the layered fringes for Ni-MoS_2 nanosheets were approximately 0.62 and 0.27 nm, which are corresponding to (002) and (100) planes of the hexagonal MoS_2 (Figure 2b). These results prove the lattice structure of Ni-MoS_2 is not changed after the Ni decoration. The HAADF-STEM image proves that there are no obvious nanoparticles or clusters, and its corresponding EDS mapping patterns confirm the successful decoration of Ni species (Figure 2c). More importantly, as shown in Figure 2d,e, the atomic resolution picture and the fast Fourier transform (FFT)-filtered image were used to characterize the Ni-MoS_2 at a sub-angstrom resolution, which demonstrates obvious defects in the Ni-MoS_2 basal plane with hexagonal structure. Moreover, some bright dots are clearly identified in the image, which are assigned to insolated

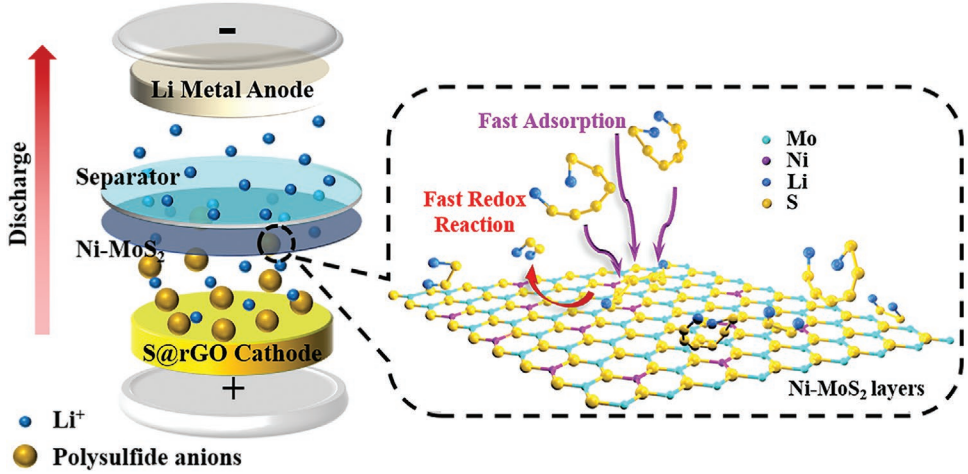

Figure 1. The schematic of the working mechanism of Ni-MoS_2 nanosheets modified separator in Li-S battery.

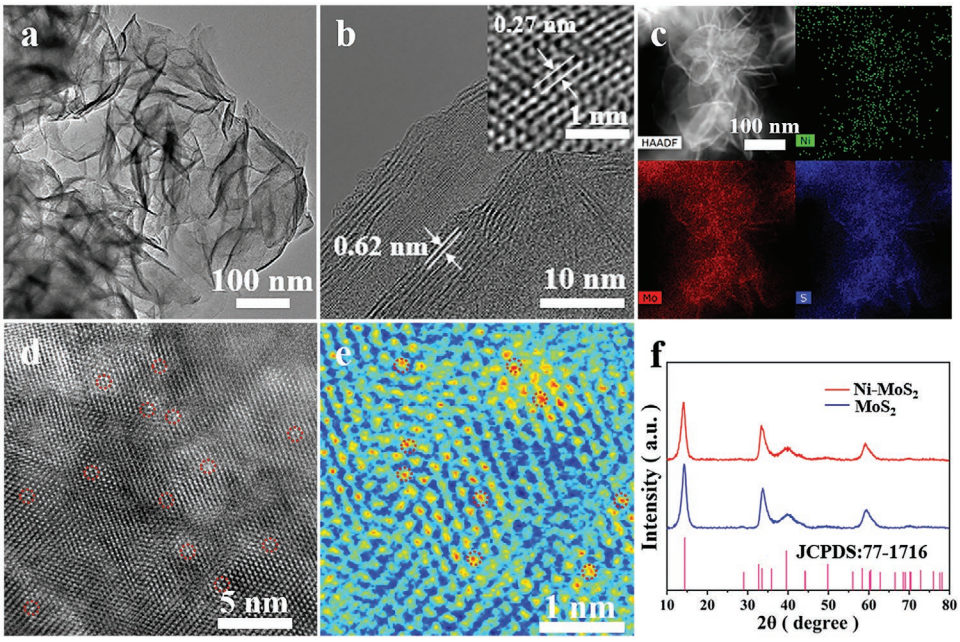

Figure 2. a) TEM images of Ni-MoS_2 nanosheets. b) HRTEM image of Ni-MoS_2 nanosheets. c) HAADF-STEM image of Ni-MoS_2 nanosheets, and its corresponding EDS mapping. d) Atomic resolution picture of the Ni-MoS_2 nanosheets and e) related FFT-filtered atomic resolution image. f) XRD patterns of Ni-MoS_2 and MoS_2 nanosheets.

Ni atoms. These results demonstrate the successful addition and uniform distribution of single Ni atoms, ensuring to catalyze polysulfides effectively and successfully. In addition, the concentration of Ni atoms is about 1.8 wt% according to the inductively coupled plasma optical emission spectroscopy (ICP-OES). Besides, XRD analysis was conducted to study the effect on the introduction of Ni atoms into MoS_2 sheets (Figure 2f). The results show no obvious difference between Ni-MoS_2 and MoS_2 nanosheets, which means no new phase is formed after doping Ni atoms.

Moreover, the electron structure and coordination environment of the Ni-MoS_2 and MoS_2 nanosheets were characterized by XPS. The Mo 3d spectrum exhibits two contributions, $3d_{5/2}$ and $3d_{3/2}$, resulting from the spin-orbit splitting, which can be assigned to MoS_2 (Figure S5a,b, Supporting Information). And there are two oxidation states, Mo^{4+} and Mo^{6+}, in the hybrids. It can be obviously observed that the higher oxidation state's peak is apparently increased due to the Ni decoration, which leads to election transfer between the single Ni atoms and MoS_2 nanosheets. In addition, the Ni 2p spectrum shows four strong peaks for differently chemical species, further confirming the existence of Ni-S band (Figure S5c, Supporting Information). These results further demonstrate the effective decoration of Ni species. In the Raman spectrum (Figure S6, Supporting Information), two different peaks are observed at 376.7 and 400.8 cm^{-1}, which correspond to in-plane Mo-S phonon mode (E^1_{2g}) and the out-of-plane Mo-S mode(A_{1g}), respectively. And the relative intensity, calculated from A_{1g}/E^1_{2g}, is increased from 1.34 (MoS_2) to 1.87 (Ni-MoS_2), which may be ascribed to the reduction of in-plane vibration after the Ni decoration.

The commercial PP separator was modified by Ni-MoS_2 via a facile slurry-coating method for further use of Li-S batteries. As shown in **Figure 3**a, the Ni-MoS_2 nanosheets were distributed evenly on the PP separator without obvious bulges (Figure S7, Supporting Information). The cross-sectional SEM image demonstrates that the thickness of the Ni-MoS_2@PP separator is around 11 µm (Figure 3b). To verify the practicability and safety of the modification separator for Li-S batteries, some physical tests for characterizing separators were conducted. Both Ni-MoS_2@PP separator and PP separator's tensile properties were compared by stress–strain curves in Figure 3c. The Ni-MoS_2@PP separator is able to endure more stress and produce greater deformation, which proves the Ni-MoS_2@PP separator possesses better mechanical property. After modified by the coating layer, the functional separator reveals good wettability by dynamic contact angle measurements (Figure 3d,e). The Ni-MoS_2@PP separator was immediately wetted and the contact angle was nearly 0° after the electrolyte was dropped on it. In contrast, the PP separator exhibited poor wettability when dropping the electrolyte. The contact angle was 30° at 0 s which is larger than Ni-MoS_2@PP separator and the angle did not change obviously after 30 s. These results indicate that the Ni-MoS_2@PP separator possesses smaller surface tension, which is beneficial for electrolyte wettability and separator stability during long cycling. In addition, the thermal stability of separators is also significant for Li-S batteries because the batteries will generate a lot of heat during the cycle inevitably, which will give rise to shrinkage and deformation of the separator and further lead to short circuit of batteries. As shown in Figure 3f, both separators were heated to 130 °C, and the Ni-MoS_2@PP separator that is put on the bottom was at a lower temperature than PP separator, which shows wonderful thermal insulation performance of Ni-MoS_2@PP separator. What is more, both Ni-MoS_2@PP separator and PP separator were put into a 120 °C oven for 24 h. The PP separator shrank obviously while Ni-MoS_2@PP separator did not show

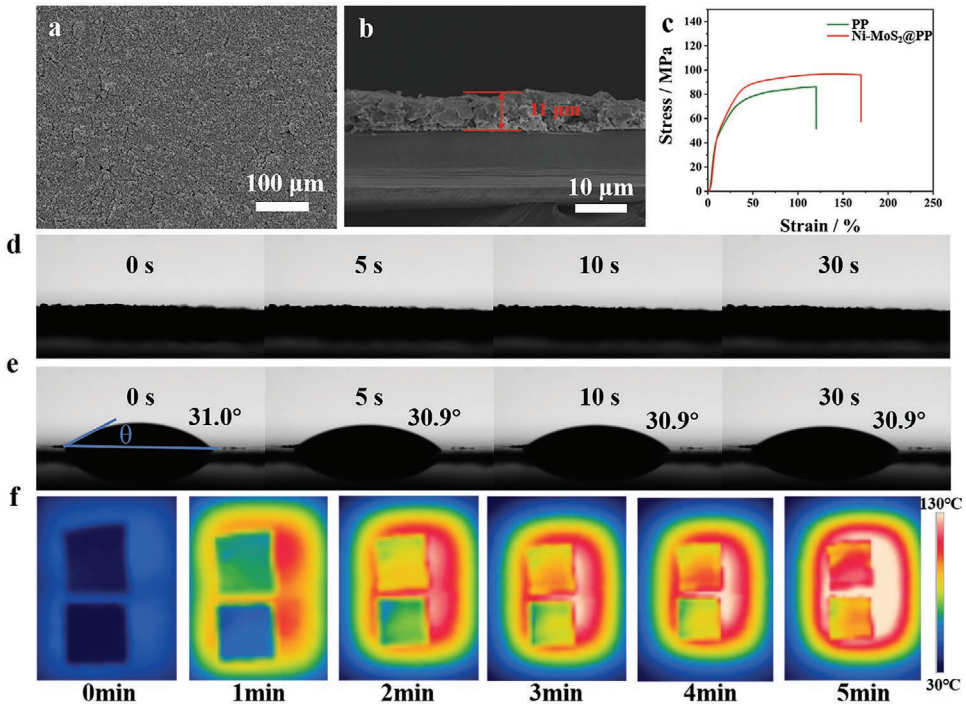

Figure 3. a) SEM image of the surface of Ni-MoS_2@PP separator. b) Cross-sectional SEM image of Ni-MoS_2@PP separator. c) Stress–strain curves of PP and Ni-MoS_2@PP separators. Contact angle measurements with electrolyte for the d) Ni-MoS_2@PP separator and e) PP separator. f) Thermal imaging photographs of Ni-MoS_2@PP and PP separators heated at 130 °C (the upper is PP separator and the below is Ni-MoS_2@PP separator).

distinct appearance in Figure S8a,b, Supporting Information. Both these results demonstrate Ni-MoS_2@PP separator has an outstanding thermal stability. Therefore, the Ni-MoS_2@PP separator exhibits excellent heat storage ability, which is instrumental in preventing heat diffusion and keeping the battery at a low temperature.

To further certify the effects of different separators on S cathode, the Li-S batteries were assembled with Ni-MoS_2, MoS_2, and PP separators. The initial cyclic voltammetry (CV) curves at a scan rate of 0.1 mV s^{-1} with the potential range of 1.7–2.8 V are presented in **Figure 4**a. For the batteries assembled with Ni-MoS_2@PP separators, two reduction peaks at 2.02 and 2.27 V can be observed during the discharge process. The first peak corresponds to the transformation from sulfur to long-chain polysulfides, while the second originates from the formation of final Li_2S or Li_2S_2 product. One anodic peak around 2.39 V is ascribed to the conversion of polysulfides to sulfur. By contrast, the reduction potential of MoS_2@PP and PP separators assembled batteries are both further away from the standard reduction potentials than the batteries with Ni-MoS_2@PP separators, which significantly verifies the improvement of the reduction of polarization by decorating Ni-MoS_2 nanosheets. What is more, three different Tafel slopes arising from CV curves were fitted to further prove the electrocatalytic performance of Li-S battery with different separators in Figure 4b,c. For the oxidation process, the Ni-MoS_2@PP separator shows the lower Tafel slope than the other two separators. As for the reduction peak corresponding to the transformation from polysulfides to Li_2S_2 and Li_2S, the Tafel slope of Ni-MoS_2@PP separator is 40 mV dec^{-1}, which is significantly lower than MoS_2@PP (62 mV dec^{-1}) and PP (119 mV dec^{-1}) separators. Combined with electrochemical AC impedance tests using symmetric cells assembled with different separators (Figure S9, Supporting Information), these results manifest strong conversion capacity of Ni-MoS_2. In addition, symmetrical batteries with different separators using Li_2S_6 electrolyte were assembled to indicate the catalytic performance. As shown in Figure 4d, the battery assembled with Ni-MoS_2@PP separator exhibits the largest response current, which further proves that the Ni-MoS_2 modified separator enhances the polysulfides conversion and redox kinetics.

The rate performance of the Li-S batteries assembled with different separators is tested with current density from 0.2 to 0.5, 1, 2, and 3 C in Figure 4e. The reversible capacities of the Li-S battery assembled with Ni-MoS_2@PP separator are 1329, 1024, 849, 751, and 677 mAh g^{-1}, respectively, which are much higher than that of MoS_2@PP and PP separator. Moreover, it still retains 991 mAh g^{-1} when the current density returns to 0.5 C, while the batteries assembled with MoS_2@PP and PP separators can only reach 553 and 372 mAh g^{-1} when the current density increases to 3 C and provide capacities of 870 and 738 mAh g^{-1} after returning to 0.5 C. These results manifest the addition of Ni atoms generates a great number of catalytic sites on Ni-MoS_2 nanosheets, which has good ability to catalyze polysulfide conversion.

In addition, the initial charge-discharge curves of batteries with Ni-MoS_2@PP separator and PP separator at 0.2 C were displayed in Figure S10, Supporting Information, for comparation. The charge-discharge polarization voltage of the battery with Ni-MoS_2@PP separator ($\eta = 0.21$ V) is much smaller than the battery with PP separator ($\eta = 0.28$ V), manifesting lower polarization. The voltage platforms of the battery with Ni-MoS_2@PP separator under different rates were shown in the Figure S11,

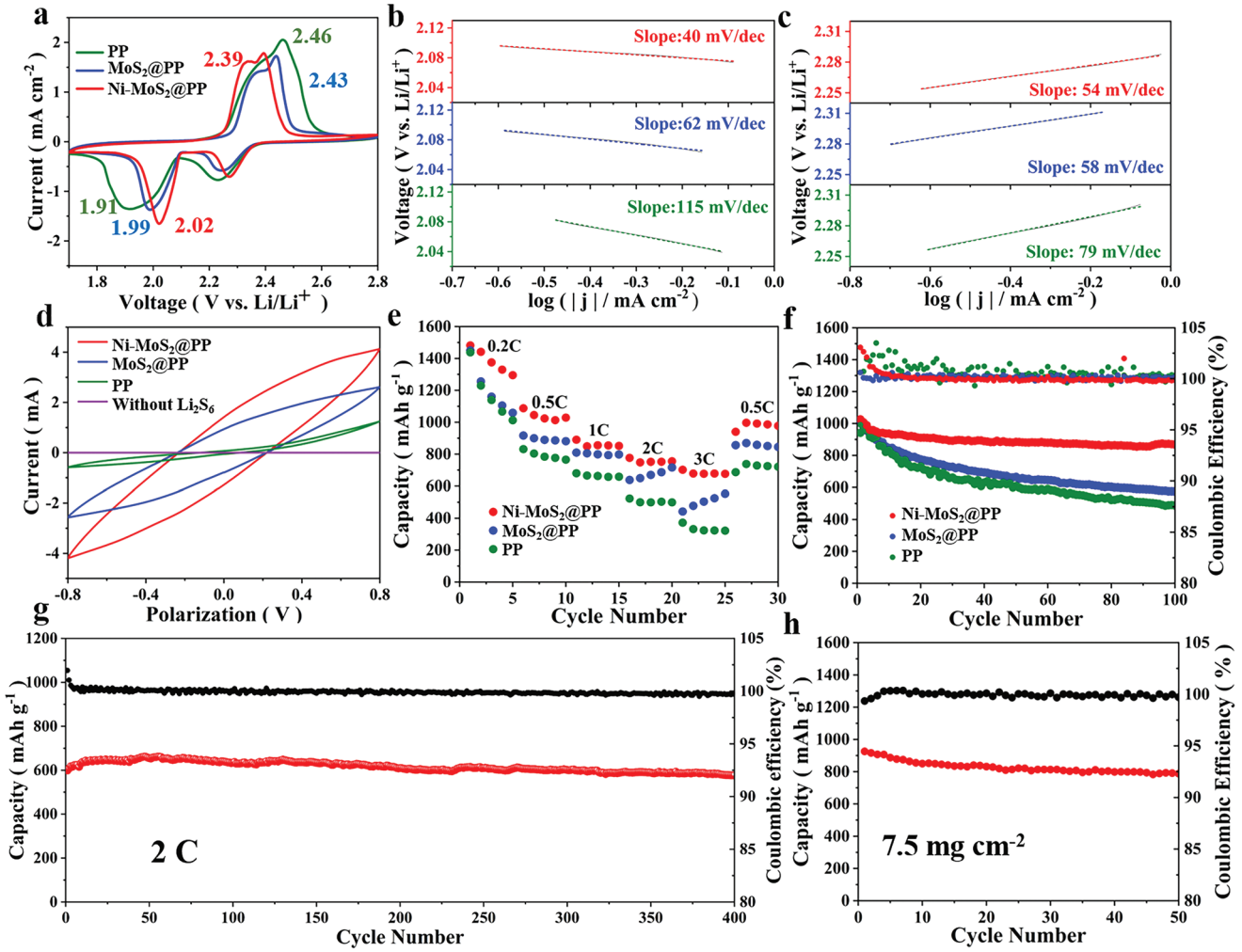

Figure 4. Electrochemical performance of the Ni-MoS_2@PP separator and its control samples. a) CV curves. b,c) Tafel slopes from the cathodic peaks of the CV curves. d) CV curves of symmetric cells. e) Rate performance. f) Cycling performance of Li-S battery with the Ni-MoS_2@PP separator at 0.5 C. g) Long-term performance of the Ni-MoS_2@PP separator at 2 C. h) Cycling performance of the Ni-MoS_2@PP separator with a high sulfur loading of 7.5 mg cm^{-2} at 0.2 C.

Supporting Information. Even at high current densities, the battery still displays two obvious discharge platform, while voltage platforms of the batteries with MoS_2@PP and PP separator are inconspicuous at high current densities (Figure S12, Supporting Information). These results suggest Ni-MoS_2@PP separator has high ion conductivity and low impedance. As shown in Figure S13, Supporting Information, the Ni-MoS_2@PP separator reveals an internal resistance (R_{ct} = 58 Ω), which is much smaller than 85 and 97 Ω of MoS_2@PP and PP separators, respectively. This outcome benefits from the facilitated polysulfide conversion and faster reaction kinetics.

The cycle performances of the Li-S batteries assembled with Ni-MoS_2@PP, MoS_2@PP, and PP separators at 0.5 C are exhibited in Figure 4f. The battery with Ni-MoS_2@PP separator shows the highest initial capacity of 1026 mAh g^{-1} and it still has a capacity of 868 mAh g^{-1} after 100 cycles. In contrast, the initial capacity of the batteries assembled with MoS_2 and PP separators are 1021 and 941 mAh g^{-1}, respectively, and only 575 and 487 mAh g^{-1} are retained after 100 cycles, respectively. In contrast to the battery with PP separator, the initial capacity of the batteries with Ni-MoS_2@PP and MoS_2@PP separator are higher, which is attributed to the adsorption of MoS_2 for inhibiting the shuttle effect of polysulfides. However, the capacity holding ability after 100 cycles of the battery with MoS_2@PP separator is worse than the battery with Ni-MoS_2@PP separator, which is ascribed to that the MoS_2@PP separators lack catalytic sites leading to sluggish redox reaction. For the Ni-MoS_2@PP separator, the addition of the single Ni atoms provides more catalytic sites to enhance the conversion of polysulfides and accordingly improves the utilization rate of sulfur. To further investigate the long cycle performance of the battery with Ni-MoS_2@PP separator, the batteries are tested at 2 C. As shown in Figure 4g, the initial capacity is 599 mAh g^{-1}. The battery exhibits excellent cycle stability with a capacity retention of 96.3% and the corresponding capacity fading rate of 0.01% per cycle after 400 cycles. As the high sulfur loading will suffer severer shuttle effect and capacity fading, for the further practical application, the cathode with high load sulfur must be investigated.

As shown in Figure 4h, even with the areal sulfur loading 7.5 mg cm^{-2}, the initial capacity of the cells is 6.9 mAh cm^{-2} at 0.2 C and retained 5.9 mAh cm^{-2} after 50 cycles at 0.2 C, which illustrates Ni-MoS_2@PP separator is able to effectively trap polysulfides and catalyze the convention of polysulfides. The above results show that Li-S batteries can be extensively enhanced using Ni-MoS_2@PP separators due to their excellent ability of adsorption and faster reaction kinetics.

To evaluate the durability and the ability to block the polysulfides of the modified separator, the Ni-MoS_2@PP separator was characterized by SEM after 20 cycles. As shown in Figure S14, Supporting Information, the coating still retains complete morphology without falling and covers the holes on the PP separator, which ensures the good stability of the Ni-MoS_2@PP separator. Moreover, in order to more intuitively observe the block effect of different separators on polysulfides, a visual observation experiment was conducted with two double-L devices. As shown in Figure S15, Supporting Information, the Li_2S_6 catholyte and blank electrolyte were separated by different separators. For PP separator, the Li_2S_6 catholyte penetrate through the PP separator gradually and it could be clearly observed the blank electrolyte became yellow after 1 h, and the color got dark as the time going due to the continuous shuttle effect of polysulfides. By comparison, for the Ni-MoS_2@PP separator, the blank electrolyte almost remained colorless after 12 h, indicating the blocking effect for the polysulfides functionally. In addition, visualized adsorption experiments were performed to characterize the ability of adsorbing polysulfides in the Figure S16, Supporting Information. The color of Li_2S_6 solution with Ni-MoS_2 was lighter than that with MoS_2 and pristine Li_2S_6 solution. And the UV–vis spectra of the Li_2S_6 solution mixed with different samples also demonstrated that Ni-MoS_2 possesses stronger adsorption ability. What is more, Li_2S nucleation experiments were conducted by in situ growing host materials on aluminum foil as an electrode matrix to prove the kinetics of nucleation and growth of Li_2S in the redox reactions from Li_2S_n to Li_2S (Figure S17, Supporting Information). The redox peaks appeared earlier for the batteries using Ni-MoS_2 electrodes (2332 s) than MoS_2 electrodes (3660 s) and the Li_2S-nucleation capacity of Ni-MoS_2 (220 mAh g^{-1}) is higher than that of MoS_2 (190 mAh g^{-1}). Consequently, these results further demonstrate the Ni-MoS_2 can effectively block and facilitate polysulfides conversion. In addition, the catalytic and adsorption effects of Ni-MoS_2 on different kinds of polysulfides and S_8 are confirmed by density functional theory (DFT) calculations. The binding energies of Ni-MoS_2 and MoS_2 are calculated for different polysulfides in **Figure 5**a,b and Figures S19 and S20, Supporting Information. The binding energies of Li_2S_4, Li_2S_6, Li_2S_8 on Ni-MoS_2 are −3.905, −3.684, and −3.298 eV, respectively, which are higher than MoS_2 for soluble long-chain polysulfides. Furthermore, the calculated Gibbs free energies for the conversion of different polysulfides for Ni-MoS_2 and MoS_2 are shown in Figure 5c. It exhibits Gibbs free energies of Ni-MoS_2 are similar with that of MoS_2 at the starting processes (Li_2S_8-Li_2S_6 and Li_2S_6-Li_2S_4), but for the limit-speed process (Li_2S_4-Li_2S_2), the Gibbs free energy of Ni-MoS_2 is significantly lower than that of MoS_2, which means the transformation tendency of this process of Ni-MoS_2 is bigger. Therefore, the lower

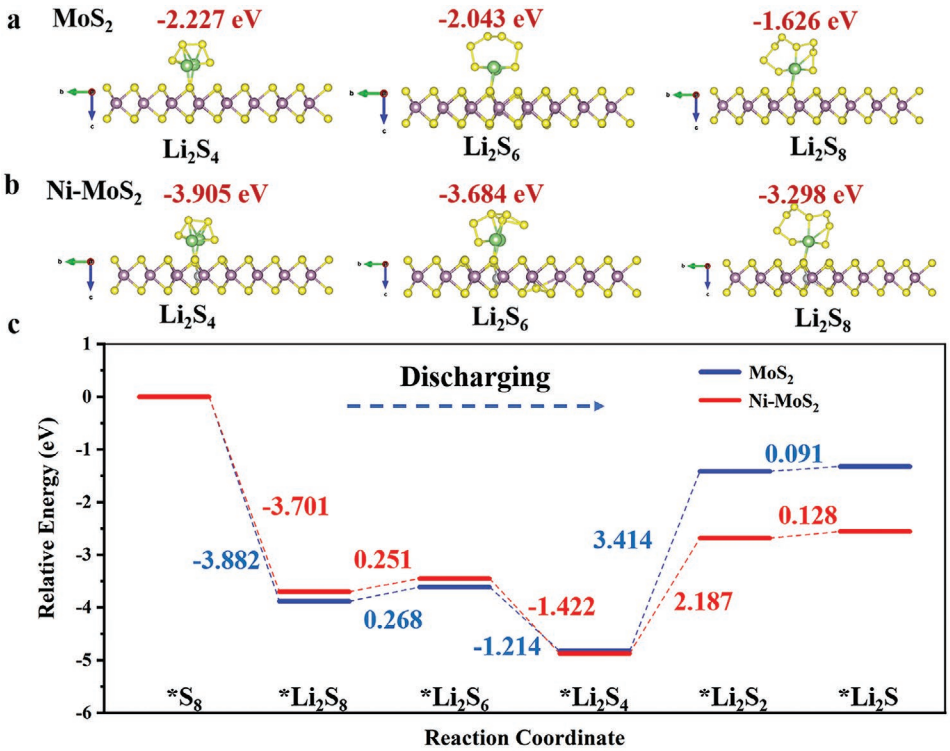

Figure 5. a,b) optimized configurations for the binding of long-chain Li_2S_n to MoS_2 and Ni-MoS_2. c) Energy profiles for the reduction of lithium polysulfides on MoS_2 and Ni-MoS_2 substrates.

Gibbs free energy suggests that the formation of Li_2S_2 is thermodynamically favorable on single Ni sites. Combined with the influence of the kinetics process, a high reduction rate could be realized on the surface of Ni-MoS_2 experimentally because of uniform active site structure, remarkable catalytic performances of Ni atoms. Therefore, Ni-MoS_2 could effectively catalyze the reduction of polysulfides. Compared with other work based on metal sulfide/single atom modifying separator in Li-S battery (Table S1, Supporting Information), this work possesses great advantages in the high sulfur loading, rate performance and cycle stability.

3. Conclusion

In conclusion, a facile synthesis method of single Ni atoms doped MoS_2 nanosheets has been adopted for separator modification and distributed single Ni atoms are verified by HAADF-STEM analysis. Moreover, the PP separator was modified by Ni-MoS_2 nanosheets with a facile coating method. The Ni-MoS_2@PP separator possesses some intrinsic advantages, such as high electrolyte uptake, good mechanical property and thermal stability, which can improve the safety of the Li-S batteries. In addition, the synergetic effect of Ni atoms and MoS_2 nanosheets can create abundant adsorptive and catalytic sites to greatly adsorb soluble long-chain polysulfides and facilitate redox kinetics. Accordingly, the Li-S batteries with Ni-MoS_2@PP separators exhibits satisfactory electrochemical performance. For example, the batteries with Ni-MoS_2@PP separators show high cycle stability over 400 cycles in high current density of 2 C and even with a high sulfur load of 7.5 mg cm^{-2}, 5.9 mAh cm^{-2} has been retained after 50 cycles. To sum up, this current work provides a new and facile method of employing single atom catalysis into polar material with good adsorption property to synergistically promote the adsorptive and catalytic performance for Li-S batteries.

4. Experimental Section

All chemicals were used as received without purification. Hexaammonium heptamolybdate tetrahydrate ($(NH_4)_6Mo_7O_{24}{\cdot}4H_2O$, HHT, 99%), thiourea (99%), nickel (II) nitrate hexahydrate were purchased from Macklin. 1,3-Dioxlane (DOL) (99.5%), 1,2-dimethoxyethane (DME) (99.5%), $LiNO_3$ (99.9%), Li_2S and sublimed sulfur power were purchased from Alfa Aesar.

Synthesis of MoS_2 and Ni-MoS_2 Nanosheets: The MoS_2 was synthesized with hydrothermal method. Initially, 1 mmol of HHT and 14 mmol thiourea were dissolved into 35 mL deionized water until the formation of a homogeneous solution. Then the obtained solution was transferred into Teflon-lined stainless-steel autoclave followed by heated in an oven at 220 °C for 24 h. Then the autoclave was cooled in fume cupboard to room temperature naturally. The product was taken out and washed several times with deionized water and ethanol to remove impurities. Then the pure product was dried at 60 °C under vacuum. For the synthesis of Ni-MoS_2 nanosheets, MoS_2 nanosheets was dispersed and stirred in the mixing solution of ethanol and deionized water followed by injecting $Ni(NO_3)_2$ solution slowly for 2 h. Finally, the products were obtained by centrifugation and drying at 60 °C under vacuum.

Preparation of Ni-MoS_2 Modified Separator: The powder of the Ni-MoS_2, acetylene black, polyvinylidene fluoride (PVDF) in *N*-methyl-2-pyrrolidone (NMP) with mass ratio 8:1:1 was mixed in the blender and then coated onto the pristine separator and dried overnight. And it was cut into a circular separator with a diameter of 17 mm.

Preparation of the S/rGO Cathode: 1.5 mg of graphene oxide, 0.069 mL sodium thiosulfate (1 mol·L^{-1}) and 0.069 mL hydrochloric acid (2 mol L^{-1}) were mixed in deionized water to obtain 1.4 mL solution in a vial. After reacted at 95 °C for 2 h, the obtained hydrogel was washed for three times by deionized water and then freeze-dried to get the freestanding S/rGO composite. The areal loading of S/rGO depended on the molar mass of sodium thiosulfate and hydrochloric acid. The sulfur content in S/rGO is 60% (Figure S18a, Supporting Information), and the sulfur loading is 2.5 mg cm^{-2} for the routine electrochemical performance test. The preparation of high sulfur loading cathodes with 7.5 mg cm^{-2} required increasing the amount of sodium thiosulfate to 0.19 mL and increases hydrochloric acid in corresponding proportion (Figure S18b, Supporting Information).

Materials Characterizations: Scanning electron microscopic (SEM) images were obtained by using a JEOL JSM-7100F at a voltage of 10 kV to get morphological information. X-ray diffraction (XRD) characterization was performed using a D8 Advance X-ray diffractometer with a non-monochromated Cu Kα X-ray source (λ = 1.054056 Å) to characterize crystallographic information of samples. Aberration-corrected high-angle annular dark field scanning transmission electron microscopy (HAADF-STEM) measurements, transmission electron microscopy (TEM), and high-resolution transmission electron microscopy (HRTEM) images were recorded with a Titan G2 60–300 with energy dispersive X-ray (EDS) image corrector. X-ray photoelectron spectroscopy (XPS) measurements were conducted using a VG MultiLab 2000 instrument.

Separator Characterizations: The dynamic contact angle measurements were conducted by using an optical contact angle measuring and contour analysis system (Dataphysics DCA 35). The tensile property measurements were conducted by an electronic universal material testing machine (Instron 5967). The heat resistance of the separator was characterized by an infrared thermal imaging camera (FLIR T429) with a temperature range from 30 to 130 °C.

Electrochemistry Measurement: Coin cells (2025-type) were assembled in an argon filled glovebox. The mechanically pressed rGO-S samples with thickness around 100 µm were directly used as the cathode, and lithium foil was utilized as anode. The electrolyte was a mixing solution of 1 M LiTFSI in DME and DOL (volume ratio 1:1), and $LiNO_3$ (1 wt%) was regarded as an additive. The ratio of electrolyte to S is 30 (µL):1 (mg). The cycling tests were performed at low current density for initial few cycles. The Galvanostatic charge/discharge cycling was conducted on Neware battery test system (CT-4008-5V6A-S1-F, Shenzhen, China) with a potential range of 1.7–2.8 V versus Li/Li^+. The cyclic voltammetry (CV) curves and electrochemical impedance spectroscopic (EIS) tests (0.1 Hz-100 kHz, 5 mV) were conducted on an electrochemical workstation (AutolabPGSTAT302N). The Li-Li symmetric cells for EIS measurements were assembled with Ni-MoS_2@PP, MoS_2 and PP separator, and 20 µL electrolyte was added to the each side.

Calculation Methods: "The first-principles calculations were performed within the density functional theory (DFT), utilizing the Vienna ab initio simulation package (VASP). The ion-electron interaction was used to describe the projected augmented wave (PAW) method and the Perdew–Burke–Ernzerhof (PBE) functional of generalized gradient approximation (GGA) was used for the exchange-correlation energy. A plane wave cutoff energy was set to be 450 eV with a precision energy of 10^{-5} eV and force criteria was less than 0.02 eV/Å on each atom. The Brillouin zone integration was performed using 2 × 2 × 1 and 8 × 8 × 4 k-point sampling. The adsorption energy is calculated due to the following formula:

$$E(ad) = E(total) - \left[E(sub) + E\left(Li_2S_{-x} \text{ or } S_8\right)\right] \quad (1)$$

where E(ad) is the bonding energy of the Li_2S_X. E(total) is the total energy of the Li_2S_X and S_8 adsorbed on the MoS_2 and Ni-MoS_2 substrate, E(sub) and E(Li_2S_X or S_8) are the energies of the substrate and the isolated molecule, respectively."

Supporting Information

Supporting Information is available from the Wiley Online Library or from the author.

Acknowledgements

C.X.D., C.Z., and Y.L. contributed equally to this work. This work was supported by National Key Research and Development Program of China (2022YFB3803502), the National Natural Science Foundation of China (52127816, 51872218), and the Fundamental Research Funds for the Central Universities (WUT: 2021IVA123, and 2021III009), the National innovation and entrepreneurship training program for college students (No. S202110497014), and Hainan Provincial Joint Project of Sanya Yazhou Bay Science and Technology City (520LH056) (all the laboratories are at WUT).

Conflict of Interest

The authors declare no conflict of interest.

Data Availability Statement

The data that support the findings of this study are available from the corresponding author upon reasonable request.;

Keywords

electrocatalysis, lithium-sulfur batteries, separators, shuttle effect

Received: September 23, 2022
Revised: November 6, 2022
Published online:

[1] J.-M. Tarascon, M. Armand, *Nature* **2001**, *414*, 359.
[2] J. R. Owen, *Chem. Soc. Rev.* **1997**, *26*, 259.
[3] D. Larcher, J.-M. Tarascon, *Nat. Chem.* **2015**, *7*, 19.
[4] G. Zhou, L. Li, D.-W. Wang, X. Shan, S. Pei, F. Li, H.-M. Cheng, *Adv. Mater.* **2015**, *27*, 641.
[5] P. G. Bruce, S. A. Freunberger, L. J. Hardwick, J.-M. Tarascon, *Nat. Mater.* **2012**, *11*, 19.
[6] X. Ji, K. T. Lee, L. F. Nazar, *Nat. Mater.* **2009**, *8*, 500.
[7] R. Fang, S. Zhao, Z. Sun, D.-W. Wang, H.-M. Cheng, F. Li, *Adv. Mater.* **2017**, *29*, 1606823.
[8] Y. Chen, H. Zhang, W. Xu, X. Yang, Y. Yu, X. Li, H. Zhang, *Adv. Funct. Mater.* **2018**, *28*, 1704987.
[9] J.-H. Kim, Y.-H. Lee, S.-J. Cho, J.-G. Gwon, H.-J. Cho, M. Jang, S.-Y. Lee, S.-Y. Lee, *Energy Environ. Sci.* **2019**, *12*, 177.
[10] C. Zhou, Q. He, Z. Li, J. Meng, X. Hong, Y. Li, Y. Zhao, X. Xu, L. Mai, *Chem. Eng. J.* **2020**, *395*, 124979.
[11] L. Luo, S.-H. Chung, Y. Asl, H. Manthiram, *Adv. Mater.* **2018**, *30*, 1804149.
[12] X. Li, J. Liang, J. Luo, C. Wang, X. Li, Q. Sun, R. Li, L. Zhang, R. Yang, S. Lu, H. Huang, X. Sun, *Adv. Mater.* **2019**, *31*, 1808100.
[13] W. Chen, T. Lei, C. Wu, M. Deng, C. Gong, K. Hu, Y. Ma, L. Dai, W. Lv, W. He, X. Liu, J. Xiong, C. Yan, *Adv. Energy Mater.* **2018**, *8*, 1702348.
[14] D. R. Deng, F. Xue, C.-D. Bai, J. Lei, R. Yuan, M. S. Zheng, Q. F. Dong, *ACS Nano* **2018**, *12*, 11120.
[15] C. Zhou, M. Chen, C. Dong, H. Wang, C. Shen, X. Wu, Q. An, G. Chang, X. Xu, L. Mai, *Nano Energy* **2022**, *98*, 107332.
[16] C.-H. Chang, S.-H. Chung, S. Nanda, A. Manthiram, *Mater. Today Energy* **2017**, *6*, 72.
[17] T.-Z. Zhuang, J.-Q. Huang, H.-J. Peng, L.-Y. He, X.-B. Cheng, C.-M. Chen, Q. Zhang, *Small* **2016**, *12*, 381.
[18] S. Bai, X. Liu, K. Zhu, S. Wu, H. Zhou, *Nat. Energy* **2016**, *1*, 16094.
[19] Q. Pang, D. Kundu, M. Cuisinier, L. F. Nazar, *Nat. Commun.* **2014**, *5*, 4759.
[20] H. B. Wu, B. Y. Xia, L. Yu, X.-Y. Yu, X. W. Lou, *Nat. Commun.* **2015**, *6*, 6512.
[21] Y. C. Jeong, J. H. Kim, S. Nam, C. R. Park, S. J. Yang, *Adv. Funct. Mater.* **2018**, *28*, 1707411.
[22] H. Shi, W. Lv, C. Zhang, D.-W. Wang, G. Ling, Y. He, F. Kang, Q.-H. Yang, *Adv. Funct. Mater.* **2018**, *28*, 1800508.
[23] D. Liu, C. Zhang, G. Zhou, W. Lv, G. Ling, L. Zhi, Q.-H. Yang, *Adv. Sci.* **2018**, *5*, 1700270.
[24] C.-Y. Fan, Y.-P. Zheng, X.-H. Zhang, Y.-H. Shi, S.-Y. Liu, H.-C. Wang, X.-L. Wu, H.-Z. Sun, J.-P. Zhang, *Adv. Energy Mater.* **2018**, *8*, 1703638.
[25] J. He, Y. Chen, A. Manthiram, *Energy Environ. Sci.* **2018**, *11*, 2560.
[26] H. Xu, D. Cheng, D. Cao, X. C. Zeng, *Nat. Catal.* **2018**, *1*, 339.
[27] Y. Wang, J. Mao, X. Meng, L. Yu, D. Deng, X. Bao, *Chem. Rev.* **2019**, *119*, 1806.
[28] X. Han, X. Ling, Y. Wang, T. Ma, C. Zhong, W. Hu, Y. Deng, *Angew. Chem., Int. Ed.* **2019**, *58*, 5359.
[29] J. Wang, L. Jia, J. Zhong, Q. Xiao, C. Wang, K. Zang, H. Liu, H. Zheng, J. Luo, J. Yang, H. Fan, W. Duan, Y. Wu, H. Lin, Y. Zhang, *Energy Storage Mater.* **2019**, *18*, 246.
[30] H. Su, L. Chen, Y. Chen, R. Si, Y. Wu, X. Wu, Z. Geng, W. Zhang, J. Zeng, *Angew. Chem., Int. Ed.* **2020**, *59*, 20411.
[31] L. Zhang, D. Liu, Z. Muhammad, F. Wan, W. Xie, Y. Wang, L. Song, Z. Niu, J. Chen, *Adv. Mater.* **2019**, *31*, 1903955.
[32] Y. Li, S. Lin, D. Wang, T. Gao, J. Song, P. Zhou, Z. Xu, Z. Yang, N. Xiao, S. Guo, *Adv. Mater.* **2020**, *32*, 1906722.
[33] Z. A. Ghazi, X. He, A. M. Khattak, N. A. Khan, B. Liang, A. Iqbal, J. Wang, H. Sin, L. Li, Z. Tang, *Adv. Mater.* **2017**, *29*, 1606817.